Fracture Mechanics of Concrete and Concrete Structures - Recent Advances in Fracture Mechanics of Concrete - B. H. Oh, et al.(eds)

Crack velocities in high-strength concrete at a wide range of loading rates

XiaoXin Zhang
Harbin Engineering University, Harbin 150001, China and E.T.S. de Ingenieros de Caminos, C. y P., Universidad de Castilla-La Mancha, 13071 Ciudad Real, Spain

Rena C. Yu, Gonzalo Ruiz, Manuel Tarifa & Miguel A. Cámara
E.T.S. de Ingenieros de Caminos, C. y P., Universidad de Castilla-La Mancha, 13071 Ciudad Real, Spain

ABSTRACT: This paper presents the recent results of an experimental program aimed at disclosing the loading rate (loading-point-displacement rate) effect on the crack velocity in high-strength concrete (HSC). Eighteen three-point-bend tests were conducted using either a servo hydraulic machine or a self-designed drop-weight impact device. Four strain gauges mounted along the ligament of the specimen were used to measure the crack velocity. Six different loading rates were applied, from 10^{-4} mm/s to 10^{3} mm/s, i.e., a low loading-rate range (5.50×10^{-4} mm/s, 0.55 mm/s and 17.4 mm/s) and a high loading-rate range (8.81×10^{2} mm/s, 1.76×10^{3} mm/s and 2.64×10^{3} mm/s). At low loading rates, the crack propagates with increasing velocity. Under high loading rates, the crack propagates with slightly decreasing velocity, though the maximum crack speed reached up to 20.6% of the Rayleigh wave speed of the tested HSC. In addition, the loading-rate effect on crack velocities is pronounced within the low loading rate regime, whereas it is minor under the high loading-rate range.

1 INTRODUCTION

Time-dependent fracture in normal strength concrete (NSC) has been the focus of many researchers for several decades. It is commonly accepted that, according to Wu and Bǎzant (Wu & Bǎzant 1993), the time-dependence of fracture is caused by three phenomena: (a) the inertia effect in the neighborhood of the crack tip, (b) the rate dependence bond-breakage process which produces the fracture surfaces, and (c) viscoelastic behavior or creep in the bulk material. The third phenomenon is negligible for very fast dynamic fracture, whilst the first one is negligible for very slow, static fracture. This has been confirmed by the fact that cohesive models endorsed with static cohesive laws successfully reproduce the dynamic fracture in quasi-brittle materials like concrete (Ruiz et al. 2000, Ruiz et al. 2001) and ceramics (Yu et al. 2004), but failed to do so in specimens loaded at low loading rates (Yu et al. 2008). For rate-dependent fracture in HSC, however, relative little experimental data is available (Müller 2008, Zhang et al. 2009). In order to gain more insight into time dependent fracture in HSC, we will concentrate on the first and second phenomenon, and endeavor to examine the fracture behavior in HSC from quasi-static to impact loading conditions. Therefore, the competing influences between the inertia effect around the crack tip and the rate-dependent process at the fracture surface is going to be our focus.

Since a characteristic and difficult feature of the rate dependence in concrete is that it is almost equally pronounced over many orders of magnitude of the loading rate, we employed a servo-hydraulic machine and a drop-weight impact machine to cover loading rates of seven orders of magnitude (from 10^{-4} mm/s to 10^{3} mm/s). In order to measure the crack-propagation velocity, we chose strain-gauge technology, which has been extensively used to investigate the deformation and crack propagation in concrete structures (Du et al. 1992, Yon et al. 1992, Xu & Reinhardt 1999, May et al. 2006, Beppu et al. 2008). Even though other common techniques, such as high-speed photography (Zehnder & Rosakis 1990, Mindess & Bentur 1985, Mindess 1995) and acoustic emission (Maji et al. 1990) are also available, they are more complicated. In particular, to cover crack propagation varying from a decimal of a mili-second to some hundreds of seconds, strain-gauge technology appears to be a more feasible solution. An additional advantage of strain-gauge technology is that, from the strain history records, we can also obtain peak strains, average strain rates and crack velocities. Such detailed information over a wide range of loading rates will undoubtedly facili-

tate the validation of numerical models aimed at disclosing rate dependency.

2 EXPERIMENTAL PROCEDURE

2.1 *Material characterization*

A single HSC was used throughout the experiments, made with porphyry aggregates of 12 mm maximum size and ASTM type IV cement, I42.5L/SR. Micro silica-fume slurry and super plasticizer (Glenium ACE 325, B255) were added to the concrete composition. The mixing proportions by weight were 1:0.336:3.52:1.62:0.3:0.043 (cement: water: coarse aggregate: sand: micro-silica fume slurry: super plasticizer).

There was a strict control of the specimen-making process to minimize scattering in test results. All of the specimens were cast in steel molds, vibrated by a vibrating table, wrap cured for 24 hours, de-molded, and stored for 4 weeks in a moist chamber at 20°C and 98% relative humidity until testing. Compressive tests were conducted according to ASTM C39 and C469 on 75 mm $\times$150 mm (diameter $\times$ height) cylinders. Brazilian tests were also carried out using cylinders of the same dimensions and following the procedures recommended by ASTM C496. Eight cylinders were cast, four for compressive tests and four for splitting tests. The mechanical properties as determined from various characterization and control tests are shown in Table1. The material's characteristic length (Eq.1) and characteristic time (Eq.2) are also listed in this table. Rayleigh wave speed υ_R is calculated as Eq.3, see Freund (Freund 1998), where υ_S is the shear wave speed.

$$l_{ch} = EG_f / f_t^2 \tag{1}$$

$$t_{ch} = l_{ch} / \upsilon_L \tag{2}$$

$$\upsilon_R = \upsilon_S (0.862 + 1.14\upsilon)/(1+\upsilon) \tag{3}$$

The characteristic length l_{ch} is pertinent to the fracture properties of a material, in a sense that, it is related to the Fracture Process Zone (FPZ) thus the brittleness of the material. For instance, the often-used Hilleborg's brittleness number is defined as D/l_{ch}, D being the beam depth or another equivalent geometric length scale. In the same way, the characteristic time t_{ch}, first introduced by Camacho & Ortiz (Camacho & Ortiz 1996), is relevant to the dynamic behavior of a cohesive material. The existence of t_{ch} enables a cohesive model endorsed with static fracture properties to discriminate between slow and fast dynamic crack propagation, see for example, (Ruiz et al. 2000, Ruiz et al. 2001,Yu et al. 2004).

Table 1. Mechanical and fracture properties of the HSC tested.

	f_c (MPa)	f_t (MPa)	G_F (N/m)	E (GPa)	ρ kg/m^3	l_{ch} (mm)	t_{ch} (μs)	v_R (m/s)
Mean	102.7	5.4	141	31	2368	150	41	2120
Std. Dev.	2	0.8	9	2	1	-	-	-

2.2 *Three-point-bend fracture tests*

As aforementioned, in order to study the loading-rate effect in HSC, three-point bending tests on notched beams were conducted over a wide range of loading rates, from 10^{-4} mm/s to 10^3 mm/s. Two testing apparatus were employed, one was a hydraulic servo-controlled testing machine, the other was a self-designed drop-weight impact instrument. The beam dimensions were 100 mm×100 mm (B×D) in cross section, and 420 mm in total length L. The initial notch-depth ratio a_0/D was approximately 0.5, and the span S was fixed at 300 mm during the tests, see Figure 1. Each specimen was removed from the moist room one day before the test and restored to the chamber after bonding the strain gauges. The specimen surface was polished and all four strain gauges (SG01-SG04, Model: LY 11 6/120A, 6 mm in length and 2.8 mm in width) were bonded to that surface, with a distance of 10 mm between each neighbouring gauge. Since a running crack in concrete is often deflected by aggregates along its path, the four strain gauges were bonded 10 mm apart from the centerline of the beam, see Figure 1. Those strain gauges provided not only the strain history at the bonded positions, but also the time at which the crack tip of the FPZ passed each strain gauge.

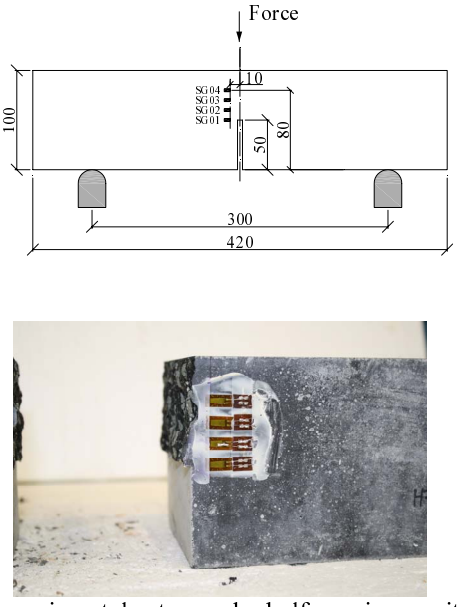

Figure 1. Experimental setup and a half-specimen with bonded strain gauges after testing (units in mm).

2.3 *Tests under loading rates from 10^{-4} mm/s to 10^{1} mm/s*

Within this low loading-rate range, the tests were performed employing the hydraulic servo-controlled testing machine under position control. Three loading rates, from quasi-static level (5.50×10^{-4} mm/s) to rate dependent levels (0.55 mm/s and 17.4 mm/s), were applied. Three specimens were tested at each loading rate. A MGCplus data acquisition system from HBM, with integrated strain amplifier and oscilloscope, was used to collect the data from the strain gauges; the sample rate was set at 2.4 kHz.

2.3.1 *Tests under loading rates from 10^{2} mm/s to 10^{3} mm/s*

Within this high loading-rate range, all tests were conducted using the instrumented, drop-weight impact apparatus, which was designed and constructed in the Laboratory of Materials and Structures at the University of Castilla-La Mancha. It has the capacity to drop a 316 kg mass from heights of up to 2.6 m, and can accommodate flexural specimens with spans of up to approximately 1.6 m. In this study, an impact hammer of 120.6 kg was employed to drop from three heights 40, 160 and 360 mm. The corresponding impact speeds were 8.81×10^{2} mm/s, 1.76×10^{3} mm/s and 2.64×10^{3} mm/s, respectively. Three specimens were tested at each impact speed. A detailed description of the instrument is given in reference (Zhang et al. 2008). The impact force is measured by a piezoelectric force sensor. In addition, the reaction force is determined by two force sensors located between the support and the specimen. A strain amplifier DEWETRON-30-8 and two oscilloscopes TDS3014B were used to acquire the data from the strain gauges, the sample rate was set at 250 kHz.

2.3.2 *Crack-velocity measurement*

When the fracture initiates, an unloading stress wave is generated and travels to the strain gauge, the sudden decrease of strain as a function of time indicates the crack initiation, see Figure 2 for a typical strain history record from one of the four strain gauges.

The crack velocity naturally refers to the speed in which this initiated cohesive crack tip, i,e. the FPZ front, will propagate. The time interval t_f is the crack initiation time. Additionally shown in Figure 2 are $t_{\varepsilon\max}$ and $t_{\varepsilon 0}$, which indicate the time at peak strain and the time at which the strain is relaxed to zero, respectively. We define the time interval between $t_{\varepsilon max}$ and $t_{\varepsilon 0}$ as the strain relaxation time t_r. Knowing $\varepsilon_{\max}$, t_f and t_r, the strain incubation rate $\dot{\varepsilon}_i$ before the strain peak and the strain relaxation rate $\dot{\varepsilon}_r$ after the strain peak can be obtained straightforwardly.

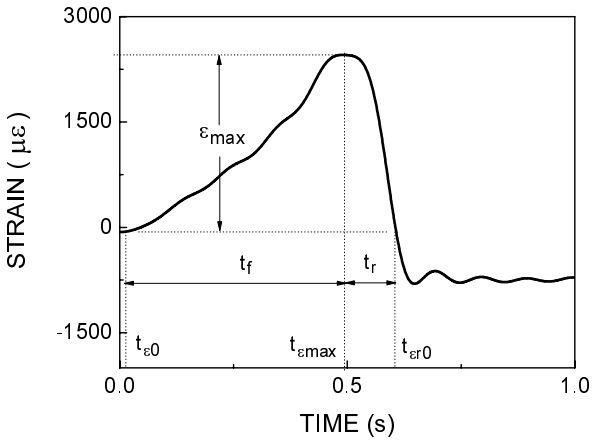

Figure 2. A typical strain versus time curve (shown in the record of SG01), taking the example of the loading rate at 0.55 mm/s.

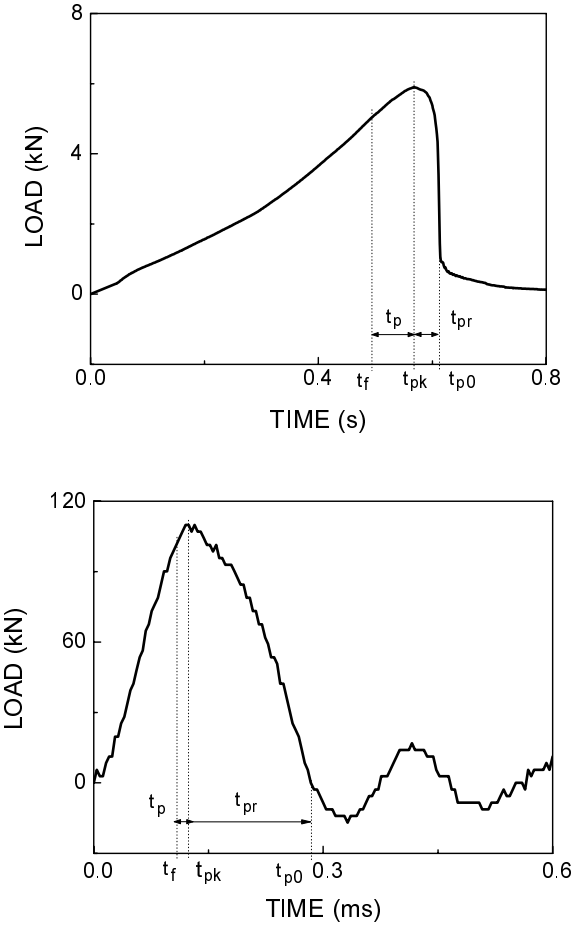

Figure 3. The typical load history for (up) low and (down) high loading rates, taking example of 0.55 mm/s and 2640 mm/s respectively.

Since the stress wave speed is much greater than the crack propagation velocity (Mindess 1995), the time taken by the unloading stress wave to propagate from the crack line to SG0n (the offset distance from the center line is 10 mm) need not be taken into account. Thus an average crack-velocity between two neighboring strain gauges can be obtained through dividing the distance in between–10 mm– by the time interval across the two corresponding peak signals recorded.

Since the peak load is an important parameter, which reflects the loading capacity of a given structural element, in our case, a three-point-bend beam, consequently all the information related to the peak load is also essential. In Figure 3, we give all the peak-load related information in two typical load history curves for low and high loading rates. The terms t_p and t_{pr} are defined as the pre- and post-peak crack propagation time. It needs to be pointed out that, unlike high loading rates, where t_{p0} is clearly seen as the intersection between the load-time curve and the time axis, at low loading rates, the load-time curve has a long tail before the load finally reaches zero, t_{p0} is taken as the time at the inflection point, see Figure 3(up). The elapsed time between $t_{\max}$ at SG04 and t_{p0} is used to obtain the crack velocity along the last 20 mm where no strain gauge was bonded. In addition, knowing the crack length at peak load a_p, the pre- and post-peak crack propagation velocity υ_1 and υ_2 are also calculated as a_p/t_p and $\left(D-a_0-a_p\right)/t_{pr}$ respectively and given in the next section.

3 RESULTS AND DISCUSSION

In order to facilitate further discussion, we give the typical strain histories recorded in gauges SG01, SG02, SG03 and SG04 at low and high loading-rates

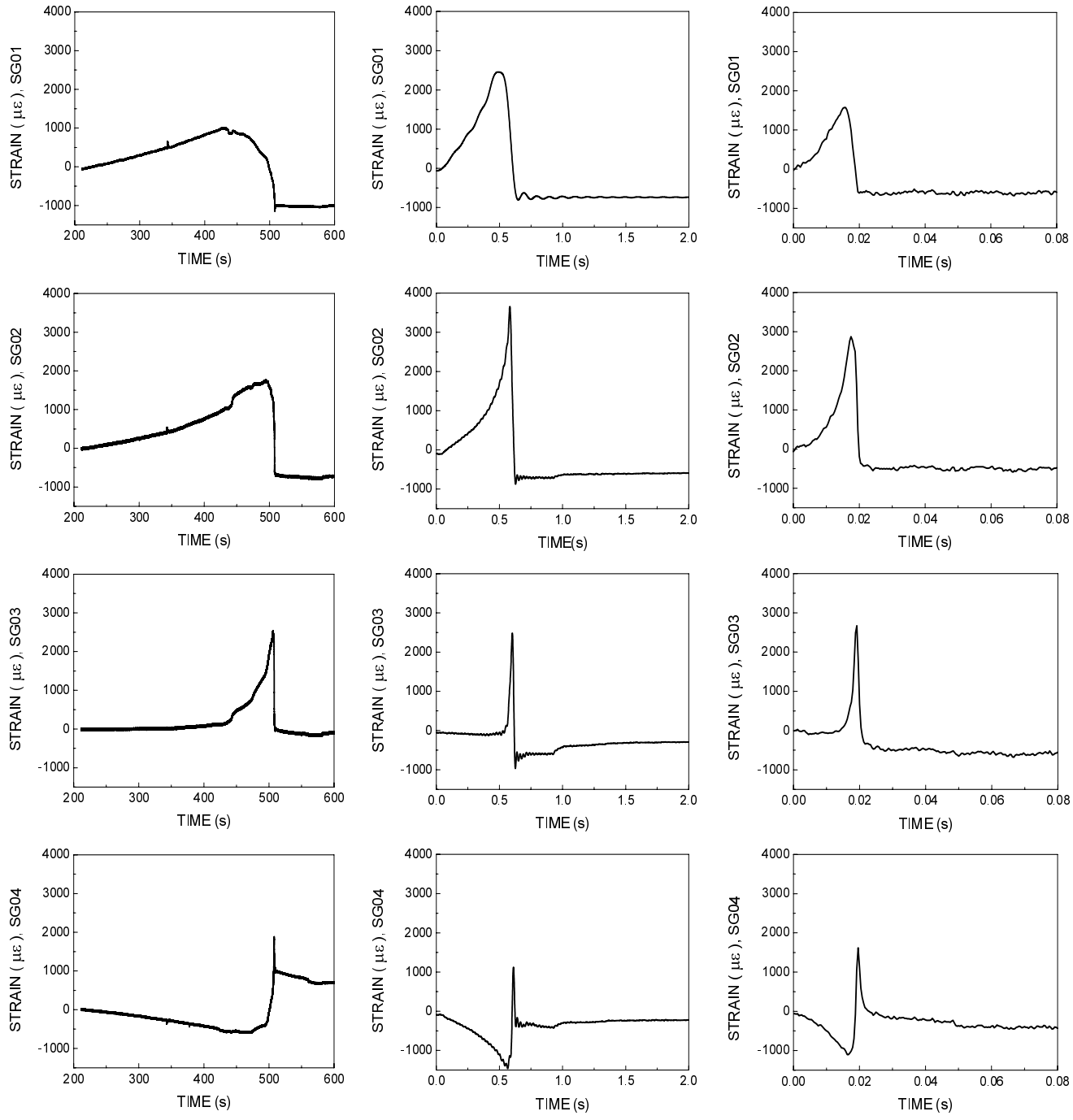

Figure 4. Strain history at loading rate of 5.5×10^{-4} (left column), 0.55 (middle column) and 17.4 (right column) mm/s.

in Figure 4 and Figure 5. Note that for each loading rate, the time axis has been initialized by offsetting $t_{\varepsilon 01}$, the time at which a first non-zero value is recorded in SG01. Please note that, the strain values of SG04 at all loading rates were negative initially, and then turned positive at a later time. This shows that, SG04 was located in a compressive zone upon loading, whereas this same zone became tensile after the crack passed.

From the strain histories, we list the peak strain $\varepsilon_{\max}$, and the time it took to arrive at peaks $t_{\varepsilon \max}$ of SG01, in Table 2 for low and high loading rates. In addition, the time at which the zero-strain is reached at postpeak, $t_{\varepsilon 0}$, the incubation rate $\dot{\varepsilon}_i = \varepsilon_{\max}/t_f$ and the relaxation rate $\dot{\varepsilon}_r = \varepsilon_{\max}/t_r$ are included in this table.

The measured load histories are depicted in Figure 6. It needs to be pointed out that under high loading rates, the load refers to the impact force, i.e., the inertial force is also included.

Information related to the peak load, such as the dynamic increase factor (DIF), the time intervals t_{pk}, t_p and t_{pr} are reported in Table 3. The measured velocities υ_{sg}, the pre- and post-peak crack propagation velocities υ_1 and υ_2 are all listed in Table 4.

3.1 *Loading-rate effect on peak strain and strain rate*

From Figure 4 and Figure 5, we observe that the values of peak strains under high loading rates are much less than those of under low loading rates. However, their values do not vary much within the low or high loading-rate range. For instance, peak strains of up to 2560, 3660 and 2870 $\mu\varepsilon$ are observed for the three low loading rates, however, peak strains of only 104.3, 66.4 and 77.2 $\mu\varepsilon$ are achieved for the high loading rates. In other words, compared to high loading rates, the deformation at low loading rates is more than one order higher. For NSC, Bǎzant & Planas (Bǎzant & Planas 1998) attributed this significant difference at peak strain to the behavior change from a domination by aggregate crack-bridging forces for a fully developed FPZ at low loading rates to a mechanism involving only a partially developed one at high loading rates. In other words, the FPZ does not have enough time to fully develop at impact loading conditions compared with that at quasi-static loading conditions.

Furthermore, we observe that, at low loading rates, t_f is inversely proportional to the loading rate, while at high loading rates, it remains almost constant. This is the main reason that the incubation rate $\dot{\varepsilon}_i$ calculated for a strain gauge located at the same distance to the notch tip, is proportional to the applied loading-rate within the low loading-rate range, while it remains practically the same under high loading-rates.

3.2 *Loading-rate effect on peak loads*

From Figure 6, note that the peak load increases proportionally with the loading rate, such rate effect is minor at low loading rates while it is pronounced at high loading rates. We define the dynamic increase factor (DIF) as the ratio of peak load and its corresponding quasi-static value (5.50×10^{-4} mm/s in this case). The DIF for peak loads are 1.4 and 25.0, for the loading rates of 17.4 mm/s and 2.64×10^{3} mm/s, respectively. In other words, the DIF at high loading rates is approximately one order higher than that at low loading rates.

It also needs to be pointed out that in Figure 6 (bottom row), we have scaled the load-axis by a factor proportional to its loading rate. Note that the peak load increases slightly faster than its loading rate. This is mainly due to the significant increase of inertia forces, see (Yu et al. 2008)

It is noteworthy that, at low loading rates, when the load peak is achieved, the crack length increased from 10 mm and 4 mm (5.5×10^{-4} and 5.5×10^{1} mm/s) to 37 mm (17.4 mm/s); while at high loading rates, the crack length varied from between 5 to 14 mm for

Table 2. Measured peak strain and strain rates for low and high loading-rates.

Loading rate (mm/s)	Strain gauges	$t_{\varepsilon 0}$ (s)	$t_{\varepsilon \max}$ (s)	t_f (s)	t_r (s)	$\mu\varepsilon_{\max}$	$\dot{\varepsilon}_i$ (10^{-6}/s)	$\dot{\varepsilon}_r$ (10^{-6}/s)
5.5×10^{-4}	SG01	0	432.5	432.5	66.2	1010	2.34	15
		(ms)	(ms)	(ms)	(ms)	$\mu\varepsilon_{\max}$	(10^{-3}/s)	(10^{-3}/s)
5.5×10^{-1}	SG01	0	490	490	115.8	2460	5.02	21
1.74×10^{1}	SG01	0	15.8	15.8	2.95	1570	99.4	532
	(μs)	(μs)	(μs)	(μs)	(μs)	$\mu\varepsilon_{\max}$	(10^{-3}/s)	(10^{-3}/s)
881	SG01	0	168	168	84	47.9	285	570
1760	SG01	0	128	128	48	53.6	419	1117
2640	SG01	0	108	108	52	61.6	570	1185

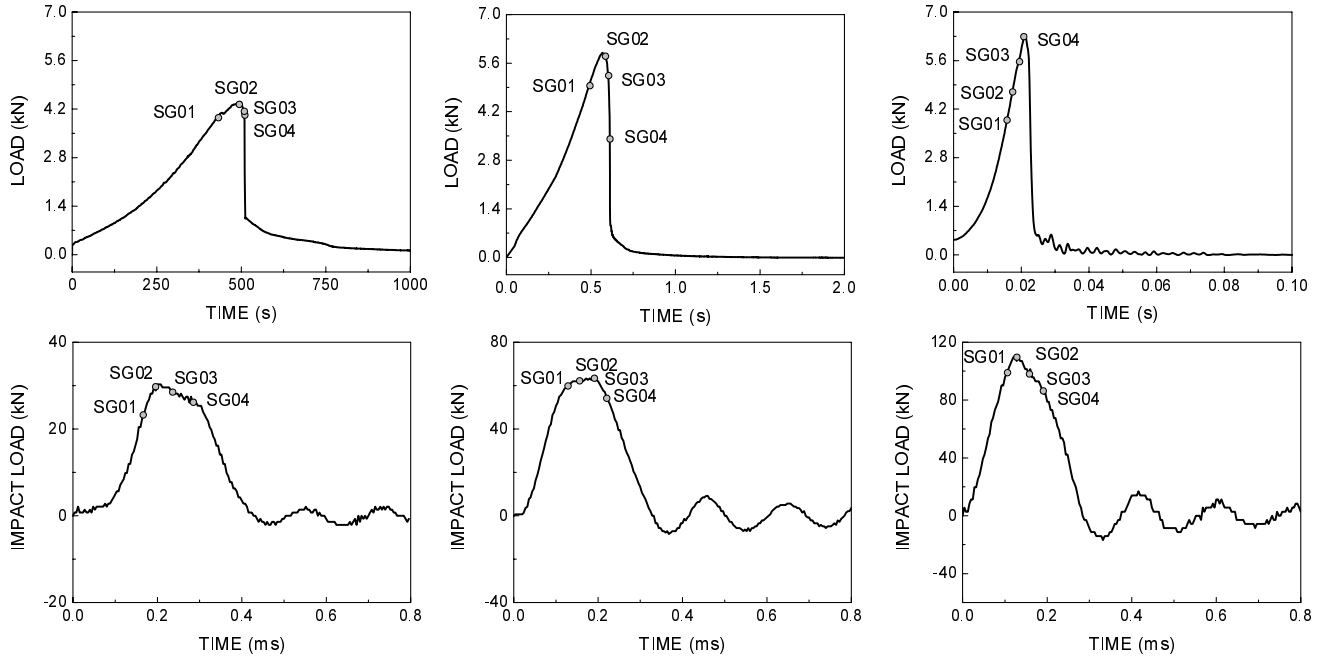

Figure 6. Load history for low loading rates (top row): 5.5×10^{-4} (left), 0.55 (middle) and 17.4 (right) mm/s, and high loading rates (bottom row): 8.81×10^{2} (left), 1.76×10^{3} (middle) and 2.64×10^{3} (right) mm/s, where SG0n marks the time at which the strain peak is obtained for strain gauge SG0n (n=1, 2, 3,4). Note that for the bottom row, the load-axis is proportionally scaled to its loading rate.

all three cases, see Table 3. In particular, for the loading rate of 17.4 mm/s, when the peak load is achieved at t_{pk} of 21 ms, SG02 is deformation free at $t_{sr\cdot02}$ of 19.9 ms, this shows the first 10-mm stretch from the notch tip is already traction free.

3.3 *Loading-rate effect on crack propagation velocity*

The crack velocities are listed in Table 4.

In the low loading rate range, on the one hand, for each loading rate, the crack advances with increasing speed; on the other hand, as the loading rate increases, the crack velocity increases proportionally. For instance, at 5.5×10^{-4} mm/s, the crack velocity increased by a factor of 38 from 0.19 mm/s for υ_{sg1} to 7.3 mm/s for υ_{sg3}; while at the loading rate of 2640 mm/s, the crack speed varied from 417 m/s to 357 m/s. When the loading rate increased by a factor of 1000 (from 5.5×10^{-4} mm/s to 0.55 mm/s), the first-stage crack velocity υ_{sg1} increased by 4100, while the late-stage velocities υ_{sg3} and υ_{sg4} only increased by a factor of 1369 and 1476 respectively. This indicates that, when the loading condition changes from quasi static to low loading rates, the loading rate effect on the early-stage crack velocity is almost three times stronger than its effect on the late-stage crack propagation; however, within the low loading rate range, when the loading rate increased by 34, from 0.55 mm/s to 17.4 mm/s, the increase factor from υ_{sg1} to υ_{sg3} remained practically the same (from 14.4 to 17.3). Within the high loading rate range, on the contrary, the crack advances with decreasing speed, and as loading rate increases, the crack propagation speed tends to be uniform, this is clearly seen from the pre and post-

Table 3. Peak load and information related to peak load.

Loading rate	*Peak load*	*DIF*	t_f	t_{pk}	t_p $(t_{pk}-t_f)$	t_{p0}	t_{pr} $(t_{p0}-t_{pk})$	a_p
(mm/s)	*(kN)*		(s)	(s)	(s)	(s)	(s)	(mm)
5.5×10^{-4}	4.4	1.0	432	494	62	512	18	10
(mm/s)	*(kN)*	-	(ms)	(ms)	(ms)	(ms)	(ms)	(mm)
5.5×10^{-1}	5.9	1.3	490	567	77	614	47	4
1.74×10^{1}	6.3	1.4	15.8	21	5.2	23.8	2.8	37
(mm/s)	*(kN)*	-	(μs)	(μs)	(μs)	(μs)	(μs)	(mm)
8.81×10^{2}	30.3	6.9	168	200	32	428.5	228.5	11
1.76×10^{3}	63.4	14.4	128	172	44	331.0	159	14
2.64×10^{3}	209.9	25.0	108	120	12	284	164	5

Table 4. Average crack velocity evolution.

Loading rate (mm/s)	v_{sg1} SG01-SG02 (m/s)	v_{sg2} SG02-SG03 (m/s)	v_{sg3} SG03-SG04 (m/s)	v_{sg4}* (m/s)	v_{max}/v_R %	Pre-peak v_1 (m/s)	Post-peak v_2 (m/s)
5.5×10^{-4}	1.9×10^{-4}	2.7×10^{-4}	7.3×10^{-3}	2.1×10^{-3}	-	2.3×10^{-4}	1.2×10^{-3}
5.5×10^{-1}	0.78	0.73	1.05	3.1	-	0.58	0.73
1.74×10^{1}	11.2	12.6	16	4.2	-	6.8	4.2
8.81×10^{2}	292	250	208	138	14.4	344	171
1.76×10^{3}	357	278	357	187	17.6	327	224
2.64×10^{3}	417	417	387	200	20.6	417	275

* V_{SG4}, crack velocity along the last 20 mm distance

peak crack velocities. The maximum crack velocity reached approximately 20.6% of the Rayleigh wave speed.

Comparing the numerically-predicted two-stage crack propagation in (Yu et al. 2008), the experimentally observed pre- and post-peak velocities in Table 4 suggest that, at low loading rates, pre-peak crack propagation is stable in a sense that, continuous loading is necessary for continuous crack advancing, whereas post-peak one is unstable, since less external load leads to faster crack propagation. On the contrary, at high loading rates, impact loads result fast crack propagation from the very beginning, less external load at post-peak is accompanied by a slower crack extension.

4 CONCLUSIONS

Using strain-gauge technology, employing a servo-hydraulic machine and a drop weight impact device, we have measured peak strains, average strain rates and crack propagation velocities for a HSC loaded over a wide range of loading rates, from 10^{-4} mm/s to 10^{3} mm/s. The following conclusions can be drawn. (a) Even though the applied loading rates covered seven orders of magnitude, the resultant initial strain rates varied from 10^{-6} to 10^{-1}/s,. (b) The peak load is sensitive to the loading rate. Under low loading rates, the rate effect on the peak load is minor, while it is pronounced under high loading rates. (c) The measured time to peak load t_{pk}, a measure of the initial CMOD rate, varied from 0.12 ms to 494 s. (d) Under low loading rates, the main crack advances with increasing velocity, the late-stage velocity is one-order higher than the early-stage one; the rate effect on the crack velocity is remarkable. At high loading rates, the main crack propagates with a decreasing crack velocity of several hundred m/s, the rate effect on crack velocity is minor. In addition the crack propagation velocity in the high loading-rate range reached 20% of the material's Rayleigh wave speed. This detailed information regarding peak strain, strain rates and crack velocities would undoubtedly facilitate the validation of numerical models aimed at evaluating the rate dependence of the fracture behavior of HSC.

ACKNOWLEDGEMENT

The authors acknowledge the financial support from the Ministerio de Fomento, (FOM/3856/2006, BOE 19/12/2006,C34/06) and the Ministerio de Ciencia e Innovación, MAT2006-09105, Spain.

REFERENCES

Bǎzant, Z. & Planas, J. (1998). Fracture and size effect in concrete and quasibrittle materials. CRC Press, Boca Ratón, Florida (USA).

Beppu, M., Miwa, K., Itoh, M., Katayama, M., & Ohno, T. (2008). Damage evaluation of concrete plates by high-velocity impact. International Journal of Impact Engineering, 35(12):1419–1426.

Camacho, G. T. & Ortiz, M. (1996). Computational modelling of impact damage in brittle materials. International Journal of Solids and Structures, 33 (20-22):2899–2938.

Du, J., Yon, J.-H., Hawkins, N., Arakawa, K. & Kobayashi, A. S. (1992). Fracture process zone for concrete for dynamic loading. ACI Materials Journal, 89(3):252–258.

Freund, L. (1998). Dynamic fracture mechanics. The Press Syndicate of the University of Cambridge.

Maji, A. K., Ouyang, C. and Shah, S. P. (1990). Fracture mechanics of quasi-brittlematerials based on acoustic emission. Materials Research Society, 5(1):206–217.

May, I. M., Chen, Y., Owen, D., Feng, Y. & Thiele, P. J. (2006). Reinforced concrete beams under drop-weight impact loads. Computers and Concrete, 3(2-3):79–90.

Mindess, S. (1995). Crack velocities in concrete subjected to impact loading. Canadian Journal of Physics, 73(5-6):310–314.

Mindess, S. and Bentur, A. (1985). A preliminary study of the fracture of concrete beams under impact loading, using high-speed photography. Cement and Concrete Research, 15(3):474–484.

Müller, H. (2008). Constitutive modelling of high strength / high performance concrete-state of the art report. CEB FIP Bulletin 42.

Ruiz, G., Ortiz, M. & Pandolfi, A. (2000). Three-dimensional finite-element simulation of the dynamic brazilian tests on concrete cylinders. International Journal for Numerical Methods in Engineering, 48:963–994.

Ruiz, G., Pandolfi, A. & Ortiz, M. (2001). Three-dimensional cohesive modelling of dynamic mixed-mode fracture. In-

ternational Journal for Numerical Methods in Engineering, 52:97–120.

Wu, Z. and Bǎzant, Z. (1993). Finite element modeling of rate effect in concrete fracture with influence of creep, In "Creep and shrinkage of concrete". Proceedings of the Fifth International RILEM Symposium, Editors, Bǎzant and Carol, pages 427–432.

Xu, S. and Reinhardt, H. (1999). Determination of double-K criterion for crack propagation in quasi-brittle fracture, Part II: Analytical evaluating and practical measuring methods for three-point bending notched beams. International Journal of Fracture, 98(2):151–177.

Yon, J.-H., Hawkins, N. M. & Kobayashi, A. (1992). Strain-rate sensitivity of concrete mechanical-properties. ACI Materials Journal, 89(2):146–153.

Yu, R., Ruiz, G. & Pandolfi, A. (2004). Numerical investigation on the dynamic behavior of advanced ceramics. Engineering Fracture Mechanics, 71:897–911.

Yu, R. C., Zhang, X. & Ruiz, G. (2008). Cohesive modeling of dynamic fracture in reinforced concrete. Computers and Concrete, 5(4):389–400.

Zehnder, A. and Rosakis, A. (1990). Dynamic fracture initiation and propagation in 4340 steel under impact loading. International Journal of Fracture, 43:271–285.

Zhang, X., Ruiz, G. & Yu, R. C. (2008). A new drop weight impact machine for studying fracture processes in structural concrete. Strain, doi: 10.1111/j.1475-1305.2008.00574.x.

Zhang, X., Ruiz, G., Yu, R. C. & Tarifa, M. (2009). Fracture behavior of highstrength concrete at a wide range of loading rates. International Journal of Impact Engineering, 36, 1204-1209.